Dielectric Surface-Controlled Low-Voltage Organic Transistors via *n*-Alkyl Phosphonic Acid Self-Assembled Monolayers on High-*k* Metal Oxide

By Orb Acton,[†] Guy G. Ting,[‡] Patrick J. Shamberger,[†] Fumio S. Ohuchi,[†] Hong Ma,*[,†] and Alex K.-Y. Jen*[,†,‡]

Department of Materials Science and Engineering, Box 352120, University of Washington, Seattle, Washington 98195-2120, and Department of Chemistry, University of Washington, Box 351700, Seattle, Washington 98195-1700

ABSTRACT In this paper, we report on n-alkyl phosphonic acid (PA) self-assembled monolayer (SAM)/hafnium oxide (HfO_2) hybrid dielectrics utilizing the advantages of SAMs for control over the dielectric/semiconductor interface with those of high-*k* metal oxides for low-voltage organic thin film transistors (OTFTs). By systematically varying the number of carbon atoms of the *n*-alkyl PA SAM from six to eighteen on HfO_2 with stable and low leakage current density, we observe how the structural nature of the SAM affects the thin-film crystal structure and morphology, and subsequent device performance of low-voltage pentacene based OTFTs. We find that two primary structural factors of the SAM play a critical role in optimizing the device electrical characteristics, namely, the order/disorder of the SAM and its physical thickness. High saturation-field-effect mobilities result at a balance between disordered SAMs to promote large pentacene grains and thick SAMs to aid in physically buffering the charge carriers in pentacene from the adverse effects of the underlying high-*k* oxide. Employing the appropriate n-alkyl PA SAM/HfO_2 hybrid dielectrics, pentacene-based OTFTs operate under −2.0 V with low hysteresis, on-off current ratios above 1×10^6, threshold voltages below −0.6 V, subthreshold slopes as low as 100 mV dec^{-1}, and field-effect mobilities as high as 1.8 $cm^2\ V^{-1}\ s^{-1}$.

KEYWORDS: self-assembled monolayer • organic semiconductor • organic field-effect transistor • hybrid materials

1. INTRODUCTION

Organic thin film transistors (OTFTs) based on π-conjugated materials are envisioned for use in ubiquitous low-cost flexible electronic devices, such as displays, sensors and electronic barcodes (1−5). A prerequisite for realizing practical applications lies on the development of stable gate dielectrics with low leakage current and high capacitance that afford low-voltage OTFT operation (6−8). In addition, for high-performance OTFTs, precise control over the chemical, electrical, and morphological properties at the organic semiconductor (OSC)/dielectric interface is required because the first few layers of the organic semiconductor in proximity to the gate dielectric are responsible for passing the majority of the current between source and drain electrodes (9−11). Therefore, studying the OSC/dielectric interface in low-voltage OTFTs is essential for developing low-power integrated circuit applications.

Standard OTFTs based on 100−300 nm SiO_2 with a dielectric constant (*k*) of 3.9 still require rather high operating voltages, often exceeding 20 V. Typically, low-voltage devices are achieved through increasing the capacitance density of the gate dielectric (C_i) by either decreasing the thickness (*d*) or increasing dielectric constant (*k*) ($C_i = \varepsilon_0 k/d$). High-*k* inorganic dielectrics (12) such as TiO_2 ($k = 21-80$) (13), titanium silicide ($k = 11-19$) (14), zirconium oxide ($k = 16-25$) (15), yitrium oxide ($k = 15-20$) (16), CeO_2 ($k \approx 26$) (17), and barium strontium titanate ($k \approx 16$) (18) to name a few, have been commonly used to achieve low-voltage OTFTs. However, these high-*k* materials adversely affect the device performance from a combination of (1) charge carrier surface trap sites associated with —OH groups (19), (2) induced ionic polarization between charge carriers and the high-*k* ionic lattice (20), and (3) surface roughness (21). To mitigate these problems, the high-*k* oxide surface is typically planarized with a polymer dielectric leaving a non-polar low-*k* surface which is generally more compatible with standard OSCs, however, with the addition of a thicker film, the C_i is reduced requiring higher driving voltages for OTFTs (22, 23).

Another promising route for low-voltage OTFTs utilizes hybrid gate dielectrics composed of self-assembled monolayers (SAMs) (24−34) or multilayers (35−37) on ultrathin inorganic oxides. SAMs are molecular films that spontaneously form by the adsorption of an organic surfactant on a solid substrate from the gas or solution phase (38−40). With the addition of a SAM just a few nm in thickness, the leakage current of a 3−4 nm thick inorganic oxide can be reduced

* Corresponding author. E-mail: ajen@u.washington.edu (A.K.-Y.J.); hma@u.washington.edu (H.M.). Tel: (206) 543-2626. Fax: (206) 543-3100.
Received for review November 4, 2009 and accepted January 5, 2010
[†] Department of Materials Science and Engineering, University of Washington.
[‡] Department of Chemistry, University of Washington.
DOI: 10.1021/am9007648

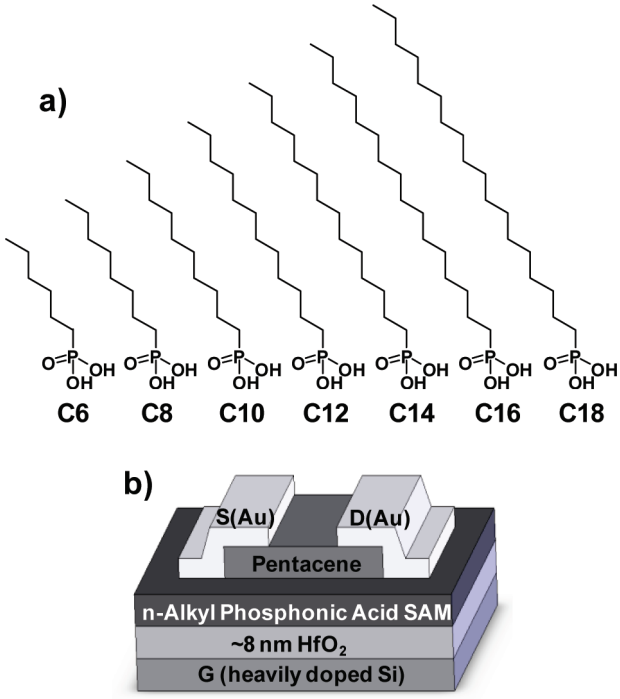

FIGURE 1. (a) Chemical structures of *n*-alkyl PA SAMs used in this study; *n*-hexylphosphonic acid (C6), *n*-octylphosphonic acid (C8), *n*-decylphosphonic acid (C10), *n*-dodecylphosphonic acid (C12), *n*-tetradecylphosphonic acid (C14), *n*-hexadecylphosphonic acid (C16), *n*-octadecylphosphonic acid (C18). (b) Schematic view of top contact OTFT using different *n*-alkyl PA SAM/hafnium oxide hybrid gate dielectrics.

to $\sim 1 \times 10^{-8}$ A cm^{-2} while still providing high capacitances above 500 nF cm^{-2} for operating voltages below 2 V (24−34). In addition, functional SAMs provide an effective method for controlling the dielectric surface properties including surface energy (24, 41, 42), chemical structure (25, 43−46), order/disorder (47−49), and molecular dipole/energy levels (50−52) that affect the thin film crystal structure and morphology, and electrical properties of the OSC and subsequent OTFT device performance. However, it is unclear whether SAMs can be used similarly as thin polymer films to effectively passivate the adverse side effects that high-*k* metal oxides have on the device performance of OTFTs. It is expected that with increased thickness, a SAM should act as a physical barrier preventing polaron coupling between the high-*k* ionic lattice and charge carriers in the OSC. However, until now, there has not been a systematic study on how the length dependence of simple alkyl chain SAMs on high-*k* metal oxides affects OSC thin film growth and OTFT device characteristics.

In this paper, we report on *n*-alkyl phosphonic acid (PA) SAM/hafnium oxide (HfO_2) hybrid dielectrics utilizing the advantages of SAMs for control over the OSC/dielectric interface with those of high-*k* metal oxides for low-voltage OTFTs. Our previous work showed that vacuum-free PA SAM/HfO_2 hybrid dielectrics posses low-leakage current, high capacitance, and a compatible OSC/dielectric interface for realizing low-voltage OTFTs (24, 25). Here, by systematically varying the alkyl chain length of the *n*-alkyl PA SAM from six to eighteen carbon atoms (Figure 1a), we observe how the structural nature of the SAM affects the low-voltage OTFT device performance. Although n-alkyl chain length dependent SAM studies on SiO_2 (47, 53) and AlO_x (26) dielectric surfaces have been demonstrated for OTFTs, SiO_2 is a low-*k* dielectric and devices operate over 20 V (47, 53), whereas possible secondary factors such as (1) the Al/AlO_x oxide roughness and (2) the thickness of the SAM and/or (3) the thickness of the AlO_x may introduce dependent OTFT electrical characteristics such as reduced field effect mobilities and on-off current ratios from high leakage currents through the hybrid gate dielectric (26). Here, we use an ultra-smooth sol−gel-processed HfO_2 with controlled thickness to provide low leakage current densities independent of the choice of the SAM. We find that two primary factors play a critical role in optimizing the device electrical characteristics using hybrid dielectrics based on SAM/high-*k* metal oxides, namely, the order/disorder of the SAM and its physical thickness. These findings give evidence that it is not only important to control how the SAM affects the thin film crystal structure and morphology of the adjacent OSC, but also how efficiently the SAM physically buffers the OSC from the adverse interactions of the underlying high-*k* dielectric.

The bottom gate-top contact device architecture used in this study is presented in Figure 1b. We use HfO_2 because of its remarkable dielectric properties, including *k* of 16−29 and wide band-gap of 5.8 eV, which is suitable for dielectrics with high capacitance and low leakage current even using films only a few nanometer in thickness (12). Seven different n-alkyl molecules were used in this study for a systematic comparison: *n*-Hexylphosphonic acid (C6), *n*-octylphosphonic acid (C8), *n*-decylphosphonic acid (C10), *n*-dodecylphosphonic acid (C12), *n*-tetradecylphosphonic acid (C14), *n*-hexadecylphosphonic acid (C16), and *n*-octadecylphosphonic acid (C18). PA headgroups of n-alkyl molecules were chosen since they readily chemisorb to metal oxides (54) with high thermal stability (400−450 °C) (55) and have several distinct advantages over their silane-based counterparts including; (1) better stability to moisture, (2) less tendency for homocondensation between PAs, and (3) the reaction between PA and the metal oxide is not limited by the content of surface hydroxyl groups (56). Pentacene was used as the organic semiconductor as it is a model compound for organic electronics and has been widely and intensively studied particularly for its use in OTFTs (57−59). The various surfaces studied in this paper are identified as follows: bare HfO_2 (BARE), HfO_2 terminated with an *n*-alkyl PA SAM (C#) where the value for "#" corresponds to the number of carbon atoms in the *n*-alkyl PA, pentacene on Bare (PEN-BARE), and pentacene on C# (PEN-C#).

2. EXPERIMENTAL SECTION

2.1. Preparation of Hafnium Oxide and Phosphonic Acid Self-Assembled Monolayers. Heavily doped p-type silicon wafers (Montco Semiconductors) were diced and cleaned in sulfuric acid:hydrogen peroxide (3:1 by volume) at 70 °C for 15 minutes, rinsed thoroughly with de-ionized (DI) water, sonicated for 15 minutes in DI water:ammonium hydroxide: hydrogen peroxide (5:1:1 by volume), rinsed and dried under nitrogen, and used immediately.

Hafnium oxide sol-gel was prepared by dissolving hafnium(IV) chloride ($HfCl_4$) (98% Aldrich) in ethanol (EtOH) under a dry nitrogen atmosphere, followed by adding a mixture of nitric acid (HNO_3) and DI water in air (molar ratio of components $HfCl_4$:EtOH:HNO_3:H_2O = 1:205:5:5). The solution was filtered using a 0.2-um PTFE filter, and heated at 50 °C for 3 h to promote hydrolysis and polymerization of HfO_x sol−gel. Hafnium oxide films were prepared by spin-coating the HfO_x sol−gel onto cleaned native oxide Si substrates at 6000 rpm for 30 s. After being left to sit for 1 h, the films were crystallized in an oven at 600 °C for 30 min, and then removed and cooled to room temperature (RT).

Phosphonic acid self-assembled monolayers were immediately prepared following HfO_2 preparation by immersing substrates into solutions of 1.0 mM of C6, C8, C10, C12, C14, C16, or C18 (PCI Synthesis) in EtOH at 70 °C. The substrates were kept in solution at 70 °C for about 15 hours followed by rinsing with EtOH, blown dry with nitrogen, and briefly baked on a hot plate at 85 °C to remove residual solvent.

2.2. Device Fabrication and Testing. Pentacene (99.995% Aldrich) was deposited at 0.2−0.3 Å s^{-1} from a resistively heated quartz crucible at 2×10^{-6} Torr, onto substrates maintained at temperatures (T_S's) of RT or 60 °C. Interdigitated source (*s*) and drain (*d*) electrodes ($W = 9000\ \mu$m, $L = 90\ \mu$m, $W/L = 100$) were defined on top of the pentacene by evaporating a 50-nm-thick gold film at 1.0 Å s^{-1} through a shadow mask from a resistively heated W boat at 2×10^{-6} Torr. All OTFT and dielectric characterization was performed under ambient conditions using an Agilent 4155B semiconductor parameter analyzer. The saturation field-effect mobility (μ) was calculated in the saturation regime from the linear fit of $(-I_{ds})^{1/2}$ versus V_{gs} using the saturation current equation: $I_{ds} = (W/2L)C_i\mu(V_{gs} - V_t)^2$ (60). The threshold voltage (V_t) was estimated as the x intercept of the linear section of the plot of $(-I_{ds})^{1/2}$ versus V_{gs}. The subthreshold swing (*S*) was calculated by taking the inverse of the slope of $-I_{ds}$ versus V_{gs} in the region of exponential current increase. Reported electrical characteristics are an average of 15 devices from three different batches. An Agilent 4192 Impedance Meter was used for capacitance characterization for frequencies from 100 Hz to 100 kHz. One-millimeter-diameter circles of thermally evaporated gold were used as the top electrode and the heavily doped silicon was used as the bottom electrode. Capacitance values were taken at 10 kHz and are an average of more than 9 devices.

2.3. Surface Characterization. Digital Instruments Multimode Nanoscope IIIa scanning probe microscope was used in Atomic Force Microscopy (AFM) taping mode. X-ray reflectivity (XRR) and X-ray diffraction (XRD) were measured using a Siemens D5000 XRD with Cu−K_α radiation ($\lambda = 1.542$ Å). An intensity versus 2θ plot (Figure 2a) was used to analyze the thickness of HfO_2 and underlying SiO_2 on Si substrates by fitting the data using the Parratt algorithm (61). XRD samples for determining the crystal structure of HfO_2 were prepared with the same conditions detailed above except the $HfCl_4$ solution used for spin-casting had a ratio of $HfCl_4$:EtOH:HNO_3:H_2O = 1:70:5:5 to provide a thick enough film for XRD measurements. Advancing contact angle values of water and diiodomethane (DIM) were measured and surface energies were calculated using the geometric-mean method (62). The reported advancing contact angle values are an average of ten measurements from two sets of samples prepared on different days with a standard deviation of ±3°. Polarized ATR-FTIR spectra were obtained using a Bruker Tensor spectrometer (Ettlingen, Germany) equipped with a nitrogen-cooled Harrick GATR single angle reflection accessory (Ossining, NY) with a spot size of 3 mm in diameter. Each spectrum was run with a minimum of 1056 scans at resolution of 4 cm^{-1} while being purged with dry nitrogen in between each data collection to eliminate water vapor from the sample compartment.

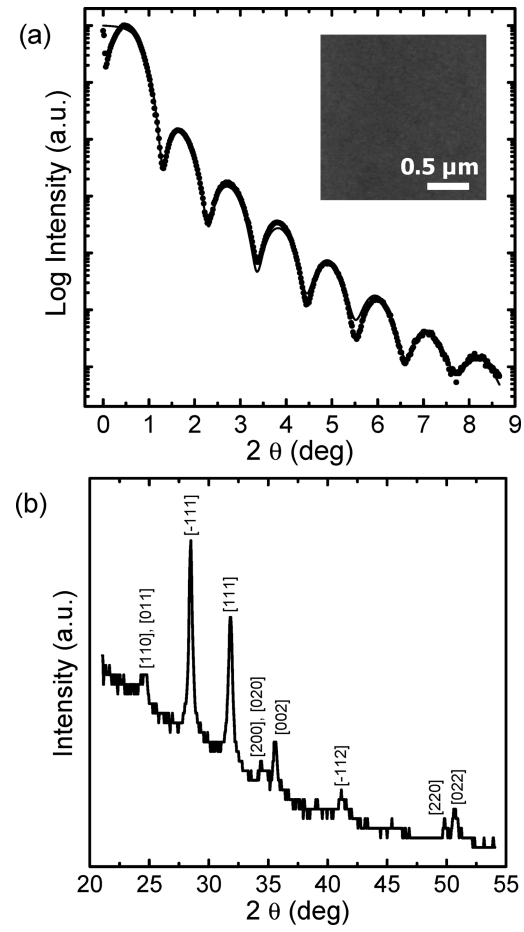

FIGURE 2. (a) Small-angle XRR of HfO_2. The solid line is the fit to the experimental data. The thickness was calculated as 8.0 nm on 2.5 nm SiO_2. Inset shows AFM topology of bare HfO_2 with color range from 0 (dark) to 5 nm (light). (b) $\theta-2\theta$ XRD of HfO_2 showing presence of monoclinic crystalline structure.

3. RESULTS AND DISCUSSION

3.1. Surface and Dielectric Characterization. We use a simple sol−gel processing technique to achieve smooth (< 0.20 nm RMS measured by AFM shown in the inset in Figure 2a) and pinhole-free HfO_2 films with easy control over the thickness below 10 nm (25). Small-angle XRR thickness measurements indicate 8.0 nm thick HfO_2 on 2.5 nm thick SiO_2 (Figure 2a), whereas $\theta-2\theta$ XRD verifies the presence of monoclinic crystalline HfO_2 (Figure 2b). After HfO_2 film formation, SAMs were prepared in EtOH solutions containing 1.0 mM of the given PA molecules at 70 °C for 16 h followed by rinsing in EtOH, drying with a stream of nitrogen, and briefly baking on a hot plate at 85 °C. AFM and ATR-FTIR were used to characterize the morphology and assess the binding modes of the n-alkyl PA SAMs assembled on HfO_2, data for C18 is included as representative of all studied *n*-alkyl PA SAMs. AFM images show that the smoothness and uniformity of the dielectric surface does not have a detectable change after SAM preparation with a smooth surface of <0.20 nm RMS (inset of Figure 3). ATR-FTIR data in the νP−O region shows the presence of a well-resolved νP═O stretch at ~1230 cm^{-1} (Figure 3). Due to the lack of evidence for other P−O region stretches, particularly those for νP−O and νP−O−H, it can be inferred that the mode of

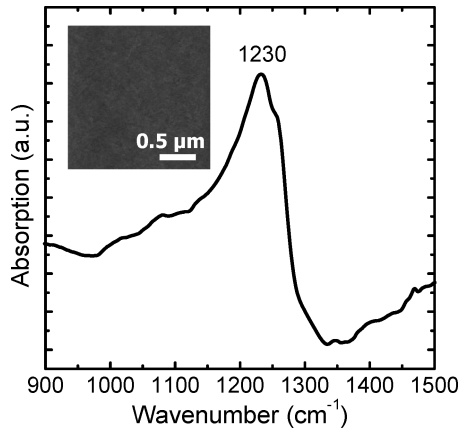

FIGURE 3. Representative ATR-FTIR spectra of νP−O region for *n*-alkyl PA SAMs showing dominant presence of νP═O at ∼1230 cm^{-1} for C18 on HfO_2. Inset shows AFM topology of C18 modified HfO_2 with color range from 0 (dark) to 5 nm (light).

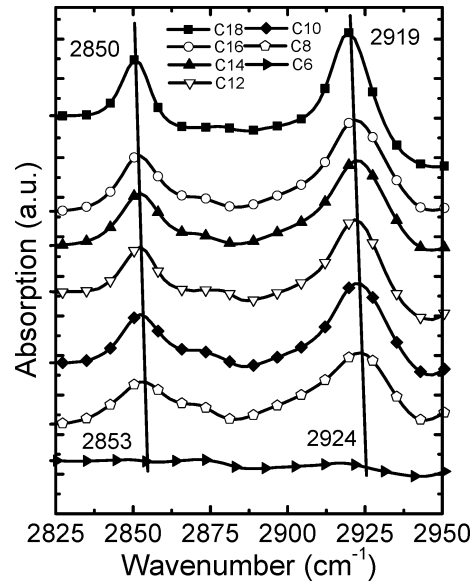

FIGURE 4. ATR-FTIR spectrum showing peak positions of symmetric (ν_s) and asymmetric (ν_a) stretching modes of methylene (CH_2) groups of the corresponding *n*-alkyl PA SAM on HfO_2. The slanted vertical lines are used to help the reader's eye.

bonding is likely bidentate, whereas there is no evidence for unbound PA headgroups or multilayers. Contact-angle goniometry using water and diiodomethane showed that through *n*-alkyl PA SAM formation, the HfO_2 surface changed from hydrophilic (<10°) and high surface energy (∼73 mJ m^{-2}) to hydrophobic (between 90 and 108°) and low surface energy (between 30 and 26 mJ m^{-2}) (Table 1). The slight decrease in water contact angle from 108° for C18 to 103° for C8, may be a result of the exposure of methylene (CH_2) groups of the shorter alkyl chains to the substrate surface. However, it is notable that the surface energies for PA SAMs from C8 to C18 are very similar and within the measurement error from contact angle goniometry (±3°). Therefore surface energy is not a significant factor when comparing OTFT device performance vide infra between different SAMs.

ATR-FTIR was used to study the organizational behavior of the n-alkyl PA SAMs on HfO_2. In the spectra of the SAM-modified substrates (Figure 4), the C−H stretches of the CH_2 group are used as the reference peaks for SAM organization (63−65). The C−H stretch has two common vibrations: a symmetric stretch, $\nu_s(CH_2)$, corresponding to a peak at ∼2850 cm^{-1} and an asymmetric stretch, $\nu_a(CH_2)$, corresponding to a peak at ∼2920 cm^{-1}. These two wavenumber values will shift to higher or lower frequencies depending on the alkyl chain conformation. When the wavenumber values shift to higher values ($\nu_a(CH_2) > 2920$ cm^{-1}), this indicates a disordered monolayer with cis interactions in the alkyl chain. When the wavenumber values shift to lower values, the monolayer is considered ordered ($\nu_a(CH_2) < 2920$ cm^{-1}) with all-trans C−C bonds. C18 has a $\nu_s(CH_2)$ of 2850 cm^{-1} and a $\nu_a(CH_2)$ 2919 cm^{-1} indicating a well ordered SAM, while C8, C10, C12, and C14 have $\nu_s(CH_2)$ and $\nu_a(CH_2)$ shifted to higher values, indicating SAMs with less order. The FTIR signal from $\nu_s(CH_2)$ and $\nu_a(CH_2)$ for C6 is very weak and therefore cannot be used to conclusively determine the structural order of this SAM. However, a water contact angle of 89° and observed smooth AFM image indicates functionalization of HfO_2 by C6. From ATR-FTIR characterization, there is a clear trend that as the length of the alkyl chain increases from C6 to C18, the order of the corresponding SAM shifts from disordered to more ordered. This is expected, as the longer chains have greater chain−chain interaction from the additive contributions of the van der Waals attractive force (∼1.5 kcal/mol per CH_2 group) resulting in more ordered self-assembly (38, 39, 65). This trend is corroborated by other *n*-alkyl chain length dependent studies of SAMs based on phosphonic acids on TiO_2 (66) and AlO_x (67), silanes on SiO_2 (47, 68), and thiols on gold (69). It is important to note that the ATR-FTIR data is averaged over a large area of the substrate (∼7 mm^2) and therefore does not by itself give information on periodic chain−chain arrangements or the structure of nanoscale heterogeneity of the corresponding SAMs. However, it is well-accepted that even highly ordered simple alkyl

Table 1. Surface Properties of Different *n*-Alkyl PA SAM/HfO_2 Hybrid Dielectrics

SAM	adv. H_2O contact angle (deg)	adv. DIM	surface energy (mJ m^{-2})	ν_a (CH_2) (cm^{-1})	ν_s (CH_2) (cm^{-1})	C_i (nF cm^{-2})	thickness (Å)
C18	108	66	26.2	2919	2850	452	21
C16	107	62	28.5	2921	2852	482	18
C14	107	67	25.3	2922	2852	504	16
C12	105	63	28.1	2922	2852	515	15
C10	104	64	27.9	2923	2853	580	10
C8	103	63	28.5	2924	2853	583	10
C6	89	59	29.9	low signal	low signal	616	8
HfO_2	<10	33	72.7			792	80

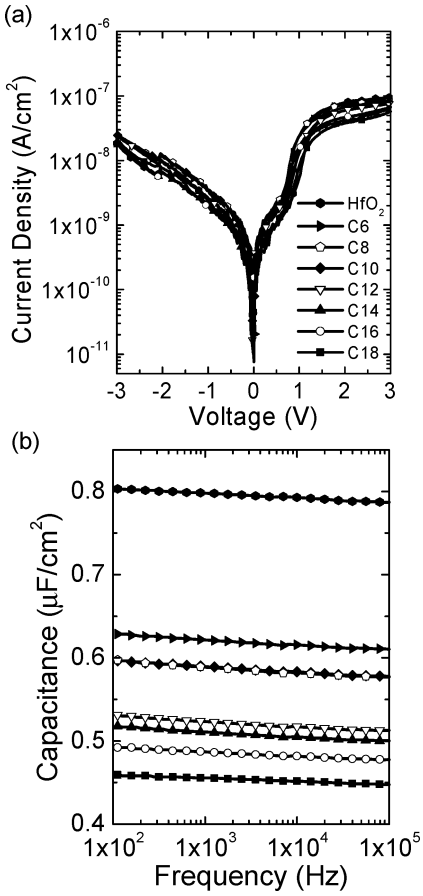

FIGURE 5. Leakage current density vs (a) voltage and capacitance density vs (b) frequency of different *n*-alkyl PA/HfO_2 hybrid dielectrics.

chain SAMs on oxide or polycrystalline metal surfaces are composed of ordered nanoscale heterogeneous domains connected by defect boundary areas with low coherence (38, 70, 71).

The leakage current densities of the different n-alkyl PA SAM/HfO_2 hybrid dielectrics are shown in Figure 5a. To ensure the OTFT electrical characteristics were independent of the adverse effects of leakage currents through the gate dielectric which can reduce field effect mobilities and on-off current ratios (26), a thick enough HfO_2 was chosen to provide stable device operation independent of the choice of the SAM. The leakage current for all the dielectrics at an applied voltage of -2 V is $\sim 1 \times 10^{-8}$ A cm^{-2}. For comparison, a control thermal oxide SiO_2 grown during the crystallization treatment of HfO_2 had a breakdown voltage of < 0.5 V.

The capacitance densities are shown in Figure 5b and summarized in Table 1. The *n*-alkyl PA/HfO_2 dielectric can be modeled as three capacitors in series ($1/C_{total} = 1/C_{SAM} + 1/C_{HfO2} + 1/C_{SiO2}$). The C_i of the control thermal oxide SiO_2 was measured as 1320 nF/cm^2 which is approximately what is expected for a 2.5 nm thick SiO_2 ($k = 3.9$). The C_i of the HfO_2 was measured as 792 nF cm^{-2}, giving a dielectric constant of 17 for the 8.0 nm film measured by XRR. The C_i of *n*-alkyl PA SAM/HfO_2 hybrid dielectrics decreased monotonically with increased length of the alkyl chain from 616 nF cm^{-2} for C6 to 452 nF cm^{-2} for C18. Assuming a dielectric constant of 2.5 for the alkyl SAM (72), the approximate thicknesses of each *n*-alkyl PA SAM was back calculated and is included in Table 1. As expected, the thickness of the SAM increases with increasing the length of the alkyl chain from approximately 8 Å for C6 to 21 Å for C18.

The combination of contact angle, AFM, FTIR, and capacitance data indicates that SAMs of *n*-alkyl PA molecules on HfO_2 range from disordered to ordered and from 8 to 21 Å in thickness as the number of carbon atoms is increased from C6 to C18. Therefore, this system is suited for observing the order/disorder and thickness dependence of a SAM on the thin film crystal structure and morphology and subsequent device performance of low-voltage pentacene OTFTs.

3.2. Pentacene Morphology and Structure. After establishing the surface and dielectric properties, pentacene films were vapor-deposited on the n-alkyl PA SAM/HfO_2 dielectrics maintained T_S values of 60 °C and RT and were then characterized by tapping-mode AFM and wide-angle XRD. Figure 6 shows the AFM images of 50-nm-thick pentacene films on different *n*-alkyl PA SAM/HfO_2 substrates. It is observable that pentacene grain size and growth mode is dependent on the order of the *n*-alkyl PA SAM. For all dielectric surfaces with BARE and disordered SAMs (C6, C8, C10, C12, C14), pentacene thin films show typical large dendritic grain formation associated with layer-plus-island growth mode (57, 58, 73). The average pentacene grain sizes on these substrates at T_S values of 60 °C and RT are 2.7 to 3.0 μm and $\sim$1.0 μm, respectively. In contrast, dielectric surfaces with ordered SAMs (C16 and C18) have small globular grains associated with island growth mode (74). The average pentacene grain sizes on these substrates at T_S values of 60 °C and RT are $\sim$1.0 μm and 100 to 150 nm, respectively.

The grain size and growth mode dependence of pentacene as a function of the order of the SAM can be explained by the growth kinetics of the first few layers of pentacene on the dielectric. It is known that the nucleation density (N) of ad-molecules is proportional to the ratio between the deposition rate (F) and the diffusion constant (D) of the molecules on the surface: $N \approx F/D$ (58, 73). Here, F is fixed at 0.3 Å/s so nucleation of pentacene grains is primarily dependent on D. With greater pentacene D, N will be suppressed, leading to larger stable nuclei and subsequently larger grain sizes. As expected, by increasing the T_S value from 25 to 60 °C, D is greater and therefore the pentacene grain size is systematically larger on all surfaces. The apparent larger D for pentacene on disordered shorter alkyl SAMs versus ordered longer alkyl SAMs requires greater discussion in detail.

Recently, it has been shown that more ordered *n*-octadecylsilane (OTS) SAMs on SiO_2 provide larger lateral crystalline SAM domains compared to disordered OTS SAMs (49). The interaction energy between ad-molecules of pentacene and ordered crystalline OTS is suggested to be responsible for the high observed N in the initial pentacene layers with the OTS crystalline domain size playing an important role

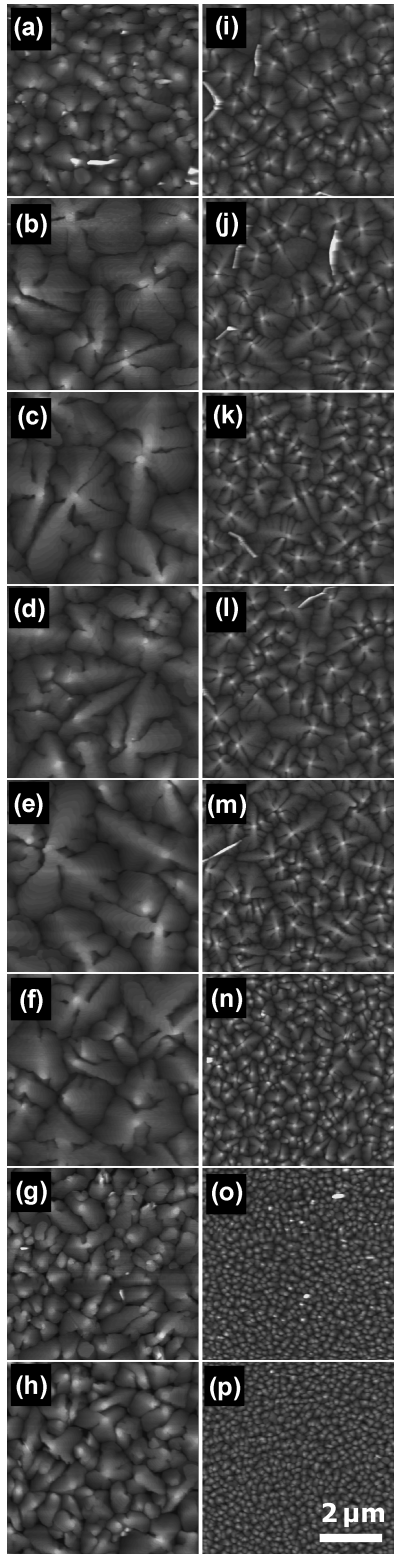

FIGURE 6. Tapping mode AFM height images of thermally evaporated 50 nm thick pentacene on substrates held at (a−h) 60 °C and (i−p) RT of (a, i) bare HfO_2 and *n*-alkyl PA SAMs of (b, j) C6, (c, k) C8, (d, l) C10, (e, m) C12, (f, n) C14, (g, o) C16, and (h, p) C18 on HfO_2. All images are 6 μm × 6 μm in size and the height ranges from 0 (dark) to 50 nm (light).

in 2D island growth (49). Quasi-epitaxial growth has been hypothesized for pentacene deposited on crystalline OTS were even though there is an absence of short range order between the pentacene thin film phase and crystalline OTS surface, long-range order can exist that may dictate the initial 2D pentacene island nucleation (48). In *n*-alkyl PA SAMs on HfO_2, we qualitatively hypothesize that the interaction energy between pentacene and more disordered shorter alkyl chains is lower than that between pentacene and more ordered longer alkyl chains. The lower interaction energy may arise from the disordered gauche defective alkyl chains providing an amorphous liquid like surface that has low interaction with pentacene versus the ordered trans-conformational alkyl chains with periodically spaced CH_3 termini providing a crystalline like surface for pentacene to find quasi-epitaxial registry on. The lower interaction energy would allow greater pentacene D and lower N, resulting in larger grain sizes on disordered shorter SAM surfaces. In addition, the more disordered shorter chain SAMs may have more amorphous domain boundaries and therefore a more amorphous homogeneous surface overall compared to highly ordered longer chain SAMs that may possess more abrupt coherency loss between crystalline domains at domain boundaries and therefore a more heterogeneous surface. The defect areas at domain boundaries in more ordered longer chain SAMs may act as greater physical energetic traps for pentacene molecules compared to the more uniform and amorphous domain boundaries of more disordered shorter chain SAMs. Therefore, the smaller pentacene grain size seen on C16 and C18 may arise from smaller pentacene D from a combination of quasi-epitaxy growth and nanoscale heterogeneity on these ordered SAMs while the larger pentacene grain sizes on C6 to C14 may arise from greater D across a more amorphous and homogeneous disordered surface.

$\theta-2\theta$ XRD scans of 50 nm thick pentacene films deposited onto *n*-alkyl PA SAM/HfO_2 substrates held at T_S values of 60 °C and RT are presented in panels a and b in Figure 7, respectively. These XRD data give only information of intermolecular order perpendicular to the substrate. Two distinct crystalline polymorphs are identified in the observed pentacene thin films; the "thin film phase", (00*l*), and "bulk phase", (00*l*)*, with d spacing of 15.4 and 14.4 Å, respectively (75−77). The coexistence of both polymorphs in pentacene is known to adversely affect the μ because structural defects between the boundaries of the two phases, such as voids, will act as scattering centers or trap sites (57, 78, 79). Theoretical calculations predict that the "thin film phase" has higher μ than the "bulk phase" because of a smaller carrier effective mass for the "thin film phase" (57, 80, 81). Typically, on bare oxide substrates with T_S = RT, only the presence of the "thin film phase" is observed using $\theta-2\theta$ XRD for films below 100 nm, while with an increased T_S, the appearance of the "bulk phase" is expected (82, 83). It is important to note that the $\theta-2\theta$ XRD data does not give information on the vertical distribution of the "thin film" and "bulk" phases in the studied pentacene films, however, from recent findings using grazing incidence XRD, the bulk phase is expected to be present even at the first few molecular layers of the film (78).

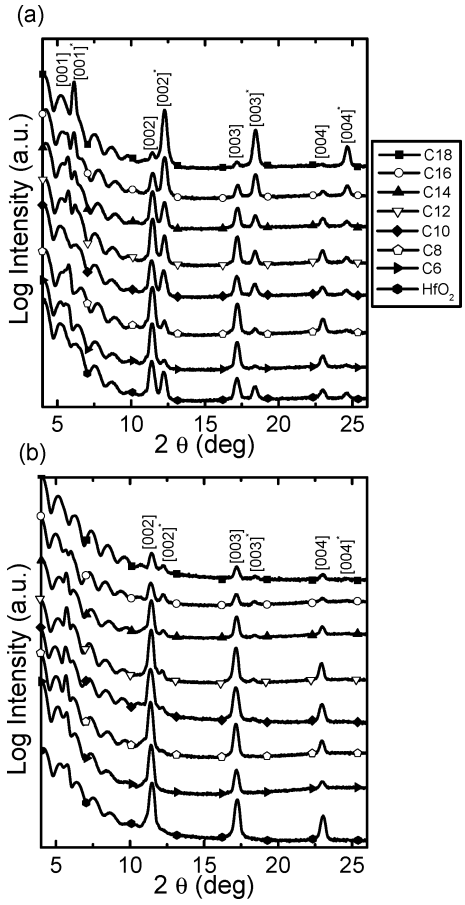

FIGURE 7. XRD data of thermally evaporated 50 nm thick pentacene on different *n*-alkyl PA SAM/HfO_2 substrates at T_S's of (a) 60 °C and (b) RT. The 001 and 001* peaks are present at 2θ angles of ~5.7 and ~6.1° but are convoluted with periodic peaks between 4 and 10° corresponding to reflections from the underlying *n*-alkyl PA/HfO_2 dielectric.

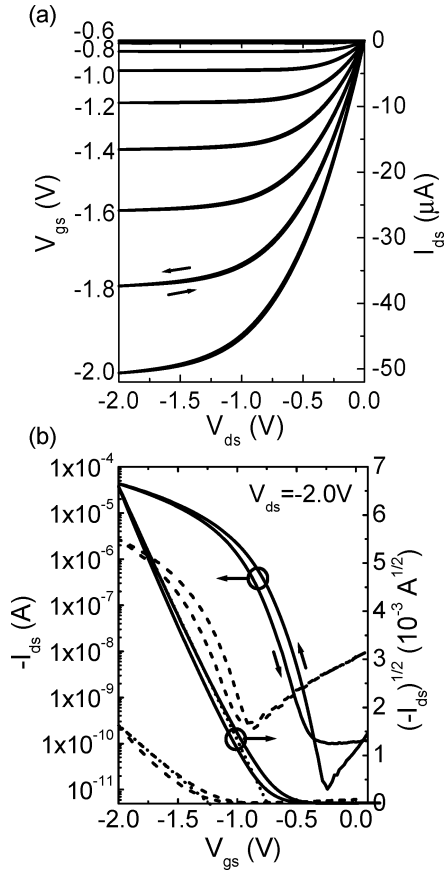

FIGURE 8. Electrical characteristics of OTFT using C8/HfO_2 hybrid dielectric and pentacene deposited at 60 °C. (a) Output characteristics (I_{ds} vs V_{ds}). (b) Transfer curve [$-I_{ds}$ vs V_{gs}, $(-I_{ds})^{1/2}$ vs V_{gs}] at a constant V_{ds} of −2.0 V for C8/HfO_2 hybrid dielectric (solid lines) and bare HfO_2 (dashed lines) (channel length = 90 μm; channel width = 9000 μm).

For pentacene films deposited at T_S = 60 °C, as the number of carbon atoms of the SAM increases from C6 to C18, the intensity of the (00*l*)* diffraction peaks increases relative to that of the (00*l*) peaks, with an abrupt change between C14 to C16 (Figure 7a and graphically represented in Figure 9c). PEN-BARE deposited at T_S 60 °C has similar intensities of both (00*l*) and (00*l*)*. Rocking curves of (00*l*) and (00*l*)* peaks indicate that the degree of orientation of the "thin film" and "bulk" phases do not change with the number of carbon atoms in the SAM. Therefore, we have interpreted changes in relative intensity of diffraction peaks to be indicative of changes in relative concentration of the two phases. In addition, pentacene films deposited at T_S = RT on BARE and C6 to C14 exhibit far greater intensity of the (00*l*) diffraction peaks compared to those deposited on C16 and C18 (Figure 7b). That we see the presence of the "bulk phase" at T_S=RT on (C10, C12, C14, C16, C18) suggested that as the SAM becomes more ordered the growth of the "bulk phase" is promoted. For both T_S = 60 °C and T_S = RT, the higher concentration of the "bulk phase" seen on more ordered SAMs (C16 and C18) versus that on more disordered SAMs (C6−C14) is concomitant with the results from AFM of island growth of small grain sizes on ordered SAMs (C16 and C18) versus layer-by-island growth of large grain sizes on more disordered SAMs (C6−C14). Similar to the above hypothesis from AFM morphology results, we believe that the formation of the "bulk phase" in pentacene films on more ordered longer chain SAMs results from a decreased *D* due to quasi-epitaxial pentacene growth and/or increased nanoscale heterogeneity of the corresponding SAM. The presence of abrupt domain boundaries in ordered longer chain SAMs may not only promote island growth but also the formation of the "bulk phase" in the corresponding thin film.

3.3. Low-Voltage OTFT Characterization. Low-voltage top contact OTFTs were fabricated by sequentially thermally evaporating pentacene and gold through shadow masks onto hybrid dielectrics. As can be seen from output and transfer curve characteristics of PEN-C8 on HfO_2 at T_S = 60 °C in Figure 8, high-quality devices with low hysteresis and operating voltages under −2.0 V are achieved by employing the *n*-alkyl SAM/HfO_2 hybrid dielectrics. For PEN-C8, device performance include, average saturation-field-effect mobilities (μ) of 1.57 cm^2 V^{-1} s^{-1} (μ_{max} = 1.8 cm^2 V^{-1} s^{-1}), on-off current ratios (I_{on}/I_{off}) greater than 1 × 10^6, threshold voltages (V_t) of −0.58 V, and low subthreshold swings (*S*) of 110 mV dec^{-1}. These are comparable to the best reported device performances for low-voltage pentacene OTFTs to date (14, 15, 28, 30, 35, 84, 85). The

Table 2. Pentacene OTFT Data for Different *n*-Alkyl PA SAMs on HfO_2[a]

SAM	μ (60 °C) ($cm^2\ V^{-1}\ s^{-1}$)	μ (RT) ($cm^2\ V^{-1}\ s^{-1}$)	V_t (V)	S ($mV\ dec^{-1}$)	I_{on}/I_{off}
C18	0.87 ± 0.09	0.25 ± 0.08	−1.06	110	1×10^6
C16	1.11 ± 0.05	0.30 ± 0.03	−0.88	110	1×10^6
C14	1.50 ± 0.12	0.82 ± 0.03	−0.86	110	1×10^6
C12	1.51 ± 0.16	1.09 ± 0.02	−0.69	100	1×10^6
C10	1.50 ± 0.08	0.84 ± 0.13	−0.59	100	1×10^6
C8	1.57 ± 0.23	0.74 ± 0.03	−0.58	110	1×10^6
C6	1.09 ±	0.56 ± 0.04	−0.56	120	1×10^6
BARE	0.28 ± 0.02	0.29 ± 0.02	−1.18	150	1×10^5

[a] Values for V_t, S, and I_{on}/I_{off} are for OTFTs with $T_S = 60$ °C.

systematic improvements in the device performance when comparing PEN-C8 to PEN-BARE (Table 2 and Figure 8b) affirms that the presence of the SAM improves the quality of the OSC/dielectric interface through interfacial modification. Lower V_t, lower S, and significantly higher μ, observed for most *n*-alkyl PA SAMs versus BARE is consistent with reducing the adverse effects of the high-*k* dielectric surface on device performance by (1) the binding of PA headgroups to —OH trap sites on the surface and (2) the physical thickness of the SAM acting to mitigate the induced ionic polarization between charge carriers and the high-*k* ionic lattice. However, when comparing OTFT results between different *n*-alkyl PA SAMs, there are variable differences particularly in μ that requires discussion in detail.

For T_S = RT, there are two systematic trends that are observable for μ when comparing different *n*-alkyl PA SAM/HfO_2 hybrid dielectrics (Table 2 and Figure 9a). These trends are as follows: (1) by increasing number of carbon atoms of the SAM from C6 to C12 there is a clear improvement in μ from 0.56 to 1.09 $cm^2\ V^{-1}\ s^{-1}$, respectively, and (2) as the number of carbon atoms in the SAM is increased further from C12 to C18 there is a precipitous reduction in μ back down to below that of BARE at 0.25 $cm^2\ V^{-1}\ s^{-1}$ for PEN-C18. For $T_S = 60$ °C, trend 1 holds for increasing the length of the SAM from C6 to C8, however, increasing the length from C8 to C14 the value for μ is relatively constant at 1.5 $cm^2\ V^{-1}\ s^{-1}$. Upon increasing the length of the SAM further from C14 to C18 for $T_S = 60$ °C, trend 2 is maintained with the observed drop in μ back down to 0.87 $cm^2\ V^{-1}\ s^{-1}$ for PEN-C18.

Of these two trends, only 2 is predictable from pentacene grain size and XRD results (Figure 9b,c). It is expected that a decrease in μ would accompany a decrease in grain size and increased relative presence of the "bulk phase" (57). The observed decrease in μ for PEN-C16 and PEN-C18 coincides with the increased order of the SAM as seen by FTIR (Figure 9d) and is corroborated by small pentacene grain size and the significantly reduced relative amount of the "thin film phase" polymorph. Our findings for trend 2 are in agreement with recent findings of pentacene deposited on ordered/disordered n-alkyl silane SAMs on SiO_2 (47). However, contrary to disordered short chain SAMs on SiO_2 showing the highest μ (47), here more disordered SAMs on high-*k*

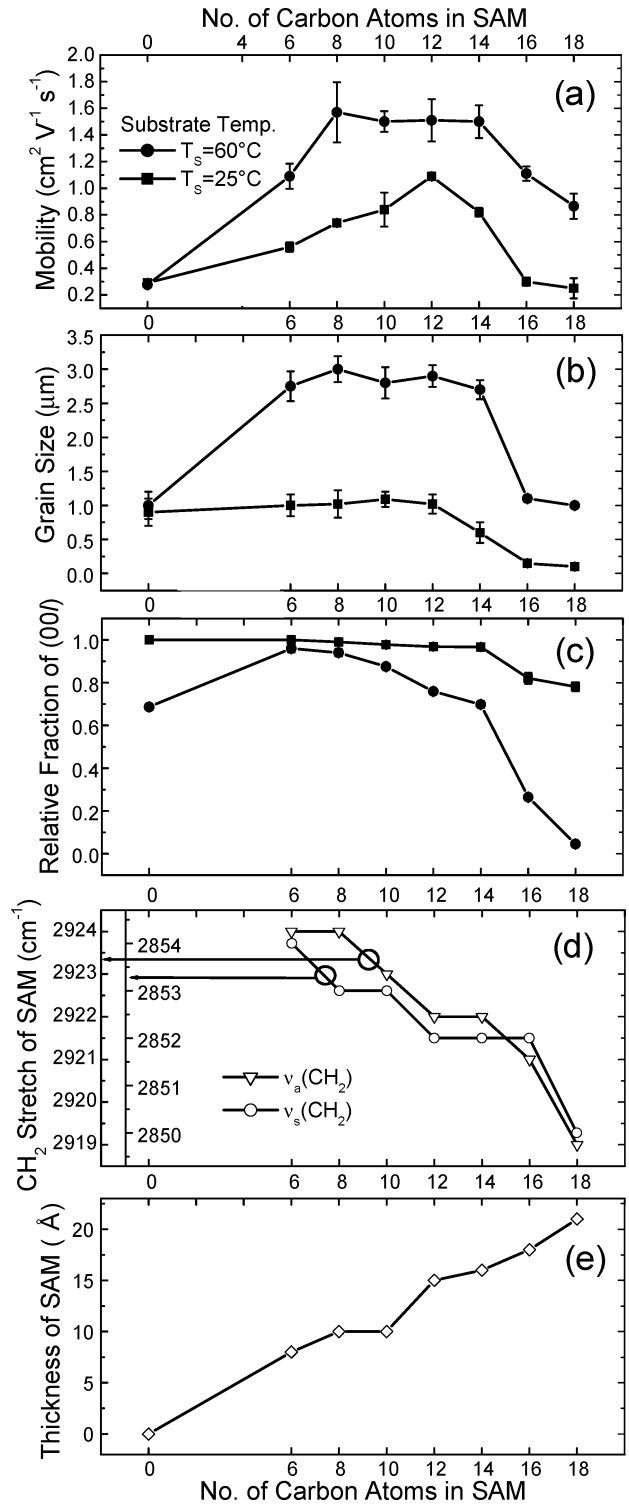

FIGURE 9. Variation in the (a) field-effect mobility in low-voltage OTFTs, (b) pentacene grain size, (c) relative fraction of (00*l*) versus (00*l*)* polymorph, (d) asymmetric [$\nu_a(CH_2)$] and symmetric [$\nu_s(CH_2)$] stretch, and (e) thickness of the SAM as a function of the number of carbon atoms in the *n*-alkyl phosphonic acid SAM on HfO_2. Data show results for pentacene deposited at T_S of 60 °C (circles) and 25 °C (squares). In c, relative fraction (R) of the (00*l*) polymorph is calculated from the average intensities (I) of the corresponding (00*l*) and (00*l*)* peaks found in Figure 7 using the equation $R = I_{(00l)}/[I_{(00l)} + I_{(00l)^*}]$. In d, data for $\nu_a(CH_2)$ and $\nu_s(CH_2)$ are used to qualitatively show how the SAMs order increases with increased number of carbon atoms.

HfO_2 do not necessarily result in the highest μ, as evident from trend 1.

Trend 1 is concomitant with an increase in the observed thickness of the SAMs from capacitance frequency measurements (Figure 9e). We hypothesize that, although the disordered nature of all SAMs from C6 to C14 promote large pentacene grain sizes, in order to achieve high μ, SAMs must also maintain a thickness above 10 Å to aid in physically buffering the highly polarizable ionic lattice of HfO_2 from forming polarons with the charge carriers in pentacene. From PEN-C6 to PEN-C12, whereas the observed increase in relative presence of the "bulk phase" should act to reduce μ, and the similar pentacene grain size between films is expected to result in similar μ, the data shows μ increasing, further corroborating the SAMs critical role as a physical buffer. That μ of PEN-C8, PEN-C10, PEN-C12, and PEN-C14 at $T_S = 60$ °C is not significantly different may result from a greater disorder of the SAM at 60 °C. It is well known that for simple alkyl SAMs, with increased temperature, more conformational disorder from gauche defects in the SAM is observed (86−88). Therefore, a greater disorder of the *n*-alkyl PA SAMs at $T_S = 60$ °C may account for the large pentacene grain size formation for PEN-C6 through PEN-C14, in turn overriding the advantageous effect of the SAMs thickness observed at $T_S =$ RT. However, as inferred from the improvement in μ comparing PEN-BARE, PEN-C6, and PEN-C8 at $T_S = 60$ °C, the presence of a disordered SAM still requires a physical thickness to block the adverse affects of the high-*k* metal oxide.

4. CONCLUSIONS

In conclusion, we have demonstrated high-performance OTFTs based on *n*-alkyl PA SAM/HfO_2 hybrid dielectrics utilizing the combined advantages of SAMs for control over the OSC/dielectric interface and high-*k* metal oxides for low-voltage operation. Employing these SAM/HfO_2 hybrid dielectrics, pentacene based OTFTs operate under −2.0 V with low hysteresis, on-off current ratios above 1×10^6, threshold voltages below −0.6 V, subthreshold slopes as low as 100 mV dec^{-1}, and field effect mobilities as high as 1.8 cm^2 V^{-1} s^{-1}. Furthermore, we have shown that by systematically varying the number of carbon atoms from C6 to C18 the OSC/dielectric interface can be controlled to tailor the low-voltage OTFT device performance. We find that high field-effect mobility comes at balance between disordered SAMs to promote large pentacene grains and a thick enough SAM to acting as a physical buffer to mitigate the adverse effects of the underlying high-*k* surface. These results provide insights for choosing suitable functional SAMs for interfacial modification in OTFTs, especially the SAMs used in low-voltage OTFTs employing SAM/ultrathin oxide hybrid dielectrics.

Acknowledgment. This work is supported by the NSF-STC program under DMR-0120967, the AFOSR program under FA9550-09-1-0426, and ONR program under N00014-08-1-1227. A.K.-Y.J. thanks the Boeing-Johnson Foundation for financial support. The authors thank the University of Washington Engineered Biomaterials Center for the use of the ATR-FTIR instrument and the Micron Foundation for their support of the XRD Facilities utilized in this study.

ARTICLE

REFERENCES AND NOTES

(1) Zaumseil, J.; Sirringhaus, H. *Chem. Rev.* **2007**, *107*, 1296–1323.
(2) Murphy, A. R.; Frechet, J. M. J. *Chem. Rev.* **2007**, *107*, 1066–1096.
(3) Jackson, T. N. *Nat. Mater.* **2005**, *4*, 581–582.
(4) Yan, H.; Chen, Z.; Zheng, Y.; Newman, C.; Quinn, J. R.; Dotz, F.; Kastler, M.; Facchetti, A. *Nature* **2009**, *457*, 679–686.
(5) Anthony, J. E. *Chem. Rev.* **2006**, *106*, 5028–5048.
(6) Facchetti, A.; Yoon, M. H.; Marks, T. J. *Adv. Mater.* **2005**, *17*, 1705–1725.
(7) Veres, J.; Ogier, S.; Lloyd, G.; de Leeuw, D. *Chem. Mater.* **2004**, *16*, 4543–4555.
(8) DiBenedetto, S. A.; Facchetti, A.; Ratner, M. A.; Marks, T. J. *Adv. Mater.* **2009**, *21*, 1407–1433.
(9) Smits, E. C. P.; Mathijssen, S. G. J.; van Hal, P. A.; Setayesh, S.; Geuns, T. C. T.; Mutsaers, K. A. H. A.; Cantatore, E.; Wondergem, H. J.; Werzer, O.; Resel, R.; Kemerink, M.; Kirchmeyer, S.; Muzafarov, A. M.; Ponomarenko, S. A.; de Boer, B.; Blom, P. W. M.; de Leeuw, D. M. *Nature* **2008**, *455*, 956–959.
(10) Horowitz, G.; Hajlaoui, R.; Bourguiga, R.; Hajlaoui, M. *Synth. Met.* **1999**, *101*, 401–404.
(11) Fritz, S. E.; Martin, S. M.; Frisbie, C. D.; Ward, M. D.; Toney, M. F. *J. Am. Chem. Soc.* **2004**, *126*, 4084–4085.
(12) Robertson, J. *Rep. Prog. Phys.* **2006**, *69*, 327–396.
(13) Majewski, L. A.; Schroeder, R.; Grell, M. *Adv. Mater.* **2005**, *17*, 192–196.
(14) Kitamura, M.; Arakawa, Y. *Appl. Phys. Lett.* **2006**, *89*, 223525.
(15) Zirkl, M.; Haase, A.; Fian, A.; Schön, H.; Sommer, C.; Jakopic, G.; Leising, G.; Stadlober, B.; Graz, I.; Gaar, N.; Schwödiauer, R.; Bauer-Gogonea, S.; Bauer, S. *Adv. Mater.* **2007**, *19*, 2241–2245.
(16) Hwang, D. K.; Kim, C. S.; Choi, J. M.; Lee, K.; Park, J. H.; Kim, E.; Baik, H. K.; Kim, J. H.; Im, S. *Adv. Mater.* **2006**, *18*, 2299–2303.
(17) Kim, C. S.; Jo, S. J.; Lee, S. W.; Kim, W. J.; Baik, H. K.; Lee, S. J. *Adv. Funct. Mater.* **2007**, *17*, 958–962.
(18) Dimitrakopoulos, C. D.; Kymissis, I.; Purushothaman, S.; Neumayer, D. A.; Duncombe, P. R.; Laibowitz, R. B. *Adv. Mater.* **1999**, *11*, 1372–1375.
(19) Chua, L. L.; Zaumseil, J.; Chang, J. F.; Ou, E. C. W.; Ho, P. K. H.; Sirringhaus, H.; Friend, R. H. *Nature* **2005**, *434*, 194–199.
(20) Hulea, I. N.; Fratini, S.; Xie, H.; Mulder, C. L.; Iossad, N. N.; Rastelli, G.; Ciuchi, S.; Morpurgo, A. F. *Nat. Mater.* **2006**, *5*, 982–986.
(21) Fritz, S. E.; Kelley, T. W.; Frisbie, C. D. *J. Phys. Chem. B* **2005**, *109*, 10574–10577.
(22) Hwang, D. K.; Lee, K.; Kim, J. H.; Im, S.; Kim, C. S.; Baik, H. K.; Park, J. H.; Kim, E. *Appl. Phys. Lett.* **2006**, *88*, 243513.
(23) Jo, S. J.; Kim, C. S.; Kim, J. B.; Kim, J.; Lee, M. J.; Hwang, H. S.; Baik, H. K.; Kim, Y. S. *Appl. Phys. Lett.* **2008**, *93*, 083504.
(24) Acton, O.; Ting, G.; Ma, H.; Hutchins, D.; Wang, Y.; Purushothaman, B.; Anthony, J. E.; Jen, A. K.-Y. *J. Mater. Chem.* **2009**, *19*, 7929–7936.
(25) Acton, O.; Ting, G.; Ma, H.; Ka, J. W.; Yip, H.-L.; Tucker, N. M.; Jen, A. K. Y. *Adv. Mater.* **2008**, *20*, 3697–3701.
(26) Jedaa, A.; Burkhardt, M.; Zschieschang, U.; Klauk, H.; Habich, D.; Schmid, G.; Halik, M. *Org. Elect.* **2009**, *10*, 1442–1447.
(27) Ma, H.; Acton, O.; Ting, G.; Ka, J. W.; Yip, H.-L.; Tucker, N.; Schofield, R.; Jen, A. K. Y. *Appl. Phys. Lett.* **2008**, *92*, 113303.
(28) Halik, M.; Klauk, H.; Zschieschang, U.; Schmid, G.; Dehm, C.; Schutz, M.; Maisch, S.; Effenberger, F.; Brunnbauer, M.; Stellacci, F. *Nature* **2004**, *431*, 963–966.
(29) Weitz, R. T.; Zschieschang, U.; Effenberger, F.; Klauk, H.; Burghard, M.; Kern, K. *Nano Lett.* **2007**, *7*, 22–27.
(30) Klauk, H.; Zschieschang, U.; Pflaum, J.; Halik, M. *Nature* **2007**, *445*, 745–748.
(31) Collet, J.; Tharaud, O.; Chapoton, A.; Vuillaume, D. *Appl. Phys. Lett.* **2000**, *76*, 1941–1943.
(32) Park, Y. D.; Kim, D. H.; Jang, Y.; Hwang, M.; Lim, J. A.; Cho, K. *Appl. Phys. Lett.* **2005**, *87*, 243509.
(33) Boulas, C.; Davidovits, J. V.; Rondelez, F.; Vuillaume, D. *Phys. Rev. Lett.* **1996**, *76*, 4797–4800.
(34) Acton, O.; Ting, G.; Ma, H.; Jen, A. K. Y. *Appl. Phys. Lett.* **2008**, *93*, 083302.
(35) DiBenedetto, S. A.; Frattarelli, D.; Ratner, M. A.; Facchetti, A.; Marks, T. J. *J. Am. Chem. Soc.* **2008**, *130*, 7528–7529.

(36) Yoon, M. H.; Facchetti, A.; Marks, T. J. *Proc. Natl. Acad. Sci. U.S.A.* **2005**, *102*, 4678–4682.
(37) Lee, B. H.; Ryu, M. K.; Choi, S. Y.; Lee, K. H.; Im, S.; Sung, M. M. *J. Am. Chem. Soc.* **2007**, *129*, 16034–16041.
(38) Love, J. C.; Estroff, L. A.; Kriebel, J. K.; Nuzzo, R. G.; Whitesides, G. M. *Chem. Rev.* **2005**, *105*, 1103–1169.
(39) Schreiber, F. *Prog. Surf. Sci.* **2000**, *65*, 151–256.
(40) Whitesides, G. M.; Grzybowski, B. *Science* **2002**, *295*, 2418–2421.
(41) Minari, T.; Kano, M.; Miyadera, T.; Wang, S.-D.; Aoyagi, Y.; Seto, M.; Nemoto, T.; Isoda, S.; Tsukagoshi, K. *Appl. Phys. Lett.* **2008**, *92*, 173301.
(42) Ball, J. M.; Wobkenberg, P. H.; Colleaux, F.; Heeney, M.; Anthony, J. E.; McCulloch, I.; Bradley, D. D. C.; Anthopoulos, T. D. *Appl. Phys. Lett.* **2009**, *95*, 103310.
(43) Kobayashi, S.; Nishikawa, T.; Takenobu, T.; Mori, S.; Shimoda, T.; Mitani, T.; Shimotani, H.; Yoshimoto, N.; Ogawa, S.; Iwasa, Y. *Nat. Mater.* **2004**, *3*, 317–322.
(44) Pernstich, K. P.; Haas, S.; Oberhoff, D.; Goldmann, C.; Gundlach, D. J.; Batlogg, B.; Rashid, A. N.; Schitter, G. *J. Appl. Phys.* **2004**, *96*, 6431–6438.
(45) McDowell, M.; Hill, I. G.; McDermott, J. E.; Bernasek, S. L.; Schwartz, J. *Appl. Phys. Lett.* **2006**, *88*, 073505.
(46) Kim, D. H.; Park, Y. D.; Jang, Y. S.; Yang, H. C.; Kim, Y. H.; Han, J. I.; Moon, D. G.; Park, S. J.; Chang, T. Y.; Chang, C. W.; Joo, M. K.; Ryu, C. Y.; Cho, K. W. *Adv. Funct. Mater.* **2005**, *15*, 77–82.
(47) Kim, D. H.; Lee, H. S.; Yang, H.; Yang, L.; Cho, K. *Adv. Funct. Mater.* **2008**, *18*, 1363–1370.
(48) Lee, H. S.; Kim, D. H.; Cho, J. H.; Hwang, M.; Jang, Y.; Cho, K. *J. Am. Chem. Soc.* **2008**, *130*, 10556–10564.
(49) Virkar, A.; Mannsfeld, S.; Oh, J. H.; Toney, M. F.; Tan, Y. H.; Liu, G.-y.; Scott, J. C.; Miller, R.; Bao, Z. *Adv. Funct. Mater.* **2009**, *19*, 1962–1970.
(50) Possanner, S. K.; Zojer, K.; Pacher, P.; Zojer, E.; Schürrer, F. *Adv. Funct. Mater.* **2009**, *19*, 958–967.
(51) Jang, Y.; Cho, J. H.; Kim, D. H.; Park, Y. D.; Hwang, M.; Cho, K. *Appl. Phys. Lett.* **2007**, *90*, 132104.
(52) Huang, C.; Katz, H. E.; West, J. E. *Langmuir* **2007**, *23*, 13223–13231.
(53) Hill, I. G.; Weinert, C. M.; Kreplak, L.; van Zyl, B. P. *Appl. Phys. A-Mater. Sci. & Proc.* **2009**, *95*, 81–87.
(54) Folkers, J. P.; Gorman, C. B.; Laibinis, P. E.; Buchholz, S.; Whitesides, G. M.; Nuzzo, R. G. *Langmuir* **1995**, *11*, 813–824.
(55) McElwee, J.; Helmy, R.; Fadeev, A. Y. *J. Coll. Inter. Sci.* **2005**, *285*, 551–556.
(56) Hanson, E. L.; Schwartz, J.; Nickel, B.; Koch, N.; Danisman, M. F. *J. Am. Chem. Soc.* **2003**, *125*, 16074–16080.
(57) Kitamura, M.; Arakawa, Y. *J. Phys.: Condens. Matter* **2008**, *20*, 184011.
(58) Ruiz, R.; Choudhary, D.; Nickel, B.; Toccoli, T.; Chang, K. C.; Mayer, A. C.; Clancy, P.; Blakely, J. M.; Headrick, R. L.; Iannotta, S.; Malliaras, G. G. *Chem. Mater.* **2004**, *16*, 4497–4508.
(59) Dimitrakopoulos, C. D.; Malenfant, P. R. L. *Adv. Mater.* **2002**, *14*, 99–117.
(60) Sze, S. M. *Physics of Semiconductor Devices*, 2nd ed.; Wiley: New York, 1981.
(61) Parratt, L. G. *Phys. Rev.* **1954**, *95*, 359.
(62) Owens, D. K.; Wendt, R. C. *J. Appl. Polym. Sci.* **1969**, *13*, 1741–1747.
(63) Allara, D. L.; Nuzzo, R. G. *Langmuir* **1985**, *1*, 45–52.
(64) Snyder, R. G.; Strauss, H. L.; Elliger, C. A. *J. Phys. Chem.* **1982**, *86*, 5145–5150.
(65) Nuzzo, R. G.; Dubois, L. H.; Allara, D. L. *J. Am. Chem. Soc.* **1990**, *112*, 558–569.
(66) Spori, D. M.; Venkataraman, N. V.; Tosatti, S. G. P.; Durmaz, F.; Spencer, N. D.; Zurcher, S. *Langmuir* **2007**, *23*, 8053–8060.
(67) Hoque, E.; DeRose, J. A.; Hoffmann, P.; Mathieu, H. J.; Bhushan, B.; Cichomski, M. *J. Chem. Phys.* **2006**, *124*, 174710.
(68) Wasserman, S. R.; Tao, Y. T.; Whitesides, G. M. *Langmuir* **1989**, *5*, 1074–1087.
(69) Porter, M. D.; Bright, T. B.; Allara, D. L.; Chidsey, C. E. D. *J. Am. Chem. Soc.* **1987**, *109*, 3559–3568.
(70) Poirier, G. E. *Chem. Rev.* **1997**, *97*, 1117–1128.
(71) Delamarche, E.; Michel, B.; Gerber, C.; Anselmetti, D.; Guntherodt, H. J.; Wolf, H.; Ringsdorf, H. *Langmuir* **1994**, *10*, 2869–2871.
(72) Fontaine, P.; Goguenheim, D.; Deresmes, D.; Vuillaume, D.; Garet, M.; Rondelez, F. *Appl. Phys. Lett.* **1993**, *62*, 2256–2258.
(73) Heringdorf, F.; Reuter, M. C.; Tromp, R. M. *Nature* **2001**, *412*, 517–520.
(74) Yang, S. Y.; Shin, K.; Park, C. E. *Adv. Funct. Mater.* **2005**, *15*, 1806–1814.
(75) Drummy, L. F.; Martin, D. C. *Adv. Mater.* **2005**, *17*, 903–907.
(76) Mattheus, C. C.; de Wijs, G. A.; de Groot, R. A.; Palstra, T. T. M. *J. Am. Chem. Soc.* **2003**, *125*, 6323–6330.
(77) Knipp, D.; Street, R. A.; Volkel, A.; Ho, J. *J. Appl. Phys.* **2003**, *93*, 347–355.
(78) Mayer, A. C.; Kazimirov, A.; Malliaras, G. G. *Phys. Rev. Lett.* **2006**, *97*, 105503.
(79) Gundlach, D. J.; Jackson, T. N.; Schlom, D. G.; Nelson, S. F. *Appl. Phys. Lett.* **1999**, *74*, 3302–3304.
(80) Doi, K.; Yoshida, K.; Nakano, H.; Tachibana, A.; Tanabe, T.; Kojima, Y.; Okazaki, K. *J. Appl. Phys.* **2005**, *98*, 113709.
(81) Parisse, P.; Ottaviano, L.; Delley, B.; Picozzi, S. *J. Phys.: Condens. Matter* **2007**, *19*, 106209.
(82) Bouchoms, I. P. M.; Schoonveld, W. A.; Vrijmoeth, J.; Klapwijk, T. M. *Synth. Met.* **1999**, *104*, 175–178.
(83) Knipp, D.; Street, R. A.; Krusor, B.; Apte, R.; Ho, J. *J. Non-Cryst. Solids* **2002**, *299*, 1042–1046.
(84) Tan, H. S.; Mathews, N.; Cahyadi, T.; Zhu, F. R.; Mhaisalkar, S. G. *Appl. Phys. Lett.* **2009**, *94*, 263303.
(85) Roberts, M. E.; Mannsfeld, S. C. B.; Queralto, N.; Reese, C.; Locklin, J.; Knoll, W.; Bao, Z. N. *Proc. Natl. Acad. Sci. U.S.A.* **2008**, *105*, 12134–12139.
(86) Lee, D. H.; Kim, D.; Oh, T.; Cho, M. *Langmuir* **2004**, *20*, 8124–8130.
(87) Gao, W.; Dickinson, L.; Grozinger, C.; Morin, F. G.; Reven, L. *Langmuir* **1997**, *13*, 115–118.
(88) Prathima, N.; Harini, M.; Rai, N.; Chandrashekara, R. H.; Ayappa, K. G.; Sampath, S.; Biswas, S. K. *Langmuir* **2005**, *21*, 2364–2374.

AM9007648